Experimental demonstration of memory-enhanced quantum communication

https://doi.org/10.1038/s41586-020-2103-5

Received: 19 August 2019

Accepted: 16 January 2020

Published online: 23 March 2020

Check for updates

M. K. Bhaskar[1], R. Riedinger[1], B. Machielse[1], D. S. Levonian[1], C. T. Nguyen[1], E. N. Knall[2], H. Park[1,3], D. Englund[4], M. Lončar[2], D. D. Sukachev[1] & M. D. Lukin[1]✉

The ability to communicate quantum information over long distances is of central importance in quantum science and engineering[1]. Although some applications of quantum communication such as secure quantum key distribution[2,3] are already being successfully deployed[4–7], their range is currently limited by photon losses and cannot be extended using straightforward measure-and-repeat strategies without compromising unconditional security[8]. Alternatively, quantum repeaters[9], which utilize intermediate quantum memory nodes and error correction techniques, can extend the range of quantum channels. However, their implementation remains an outstanding challenge[10–16], requiring a combination of efficient and high-fidelity quantum memories, gate operations, and measurements. Here we use a single solid-state spin memory integrated in a nanophotonic diamond resonator[17–19] to implement asynchronous photonic Bell-state measurements, which are a key component of quantum repeaters. In a proof-of-principle experiment, we demonstrate high-fidelity operation that effectively enables quantum communication at a rate that surpasses the ideal loss-equivalent direct-transmission method while operating at megahertz clock speeds. These results represent a crucial step towards practical quantum repeaters and large-scale quantum networks[20,21].

Efficient, long-lived quantum memory nodes are expected to play an essential part in extending the range of quantum communication[9], as they enable asynchronous quantum logic operations, such as Bell-state measurements (BSMs), between optical photons. Such an asynchronous BSM is central to many quantum communication protocols, including the realization of scalable quantum repeaters[9] with multiple intermediate nodes. Its elementary operation can be understood by considering a specific implementation of quantum cryptography[22,23] illustrated in Fig. 1a. Here two remote communicating parties, Alice and Bob, try to agree on a key that is secure against potential eavesdroppers. They each send a randomly chosen photonic qubit $\{|\pm x\rangle, |\pm y\rangle\}$ encoded in one of two conjugate bases (X or Y) across a lossy channel to an untrusted central node (Charlie), who performs a BSM and reports the result over an authenticated public channel. After a number of iterations, Alice and Bob publicly reveal their choice of bases to obtain a correlated bit string (a sifted key) from the cases when they used a compatible basis. A potentially secure key can subsequently be distilled provided the BSM error rate is low enough.

Although a photonic BSM can be implemented with linear optics and single-photon detectors, the BSM is only successful in this 'direct-transmission' approach when photons from Alice and Bob arrive simultaneously. Thus, when Alice and Bob are separated by a lossy fibre with a total transmission probability $p_{A\to B} \ll 1$, Charlie measures photon coincidences with probability also limited by $p_{A\to B}$, leading to a fundamental bound[8] on the maximum possible distilled key rate of $R_{max} = p_{A\to B}/2$ bits per channel use for an unbiased basis choice[4]. Although linear optical techniques to circumvent this bound are now being actively explored[24], they offer only limited improvement and cannot be scaled beyond a single intermediate node.

Alternatively, this bound can be surpassed using a quantum memory node at Charlie's location. In this approach, illustrated in Fig. 1b, the state of Alice's photon is stored in the heralded memory while awaiting receipt of Bob's photon over the lossy channel. Once the second photon arrives, a BSM between Alice's and Bob's qubits yields a distilled key rate that for an ideal memory scales as[25] $R_s \propto \sqrt{p_{A\to B}}$, potentially leading to substantial improvement over direct transmission.

Efficient nanophotonic quantum node

In this work we realize and use a quantum node that enables BSM rates exceeding those of an ideal system based on linear optics. We focus on the demonstration and characterization of the BSM node, leaving the implementation of source-specific technical components of full-scale quantum key distribution systems, such as decoy states[26], basis biasing[27], a finite key error analysis[28] and a physical separation of Alice and Bob for future work. Our realization is based on a single silicon–vacancy (SiV) colour centre integrated inside a diamond nanophotonic cavity[17–19] (Fig. 2a). Its key figure-of-merit, the cooperativity[13] C, describes the ratio of the interaction rate with individual cavity photons compared to all dissipation rates. A low mode volume $(0.5(\lambda/n)^3$, with wavelength λ and refractive index n), high quality factor (2×10^4), and nanoscale positioning of SiV centres enable an exceptional $C = 105 \pm 11$. Cavity photons at 737 nm wavelength are critically coupled to a waveguide

[1]Department of Physics, Harvard University, Cambridge, MA, USA. [2]John A. Paulson School of Engineering and Applied Sciences, Harvard University, Cambridge, MA, USA. [3]Department of Chemistry and Chemical Biology, Harvard University, Cambridge, MA, USA. [4]Research Laboratory of Electronics, MIT, Cambridge, MA, USA. ✉e-mail: lukin@physics.harvard.edu

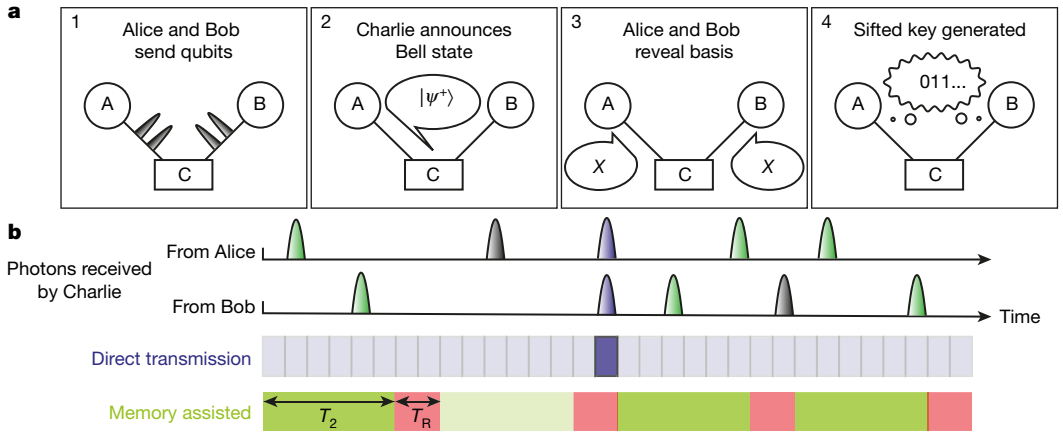

Fig. 1 | Concept of memory-enhanced quantum communication. **a**, Quantum communication protocol. Alice and Bob (A and B, respectively) send qubits encoded in photons to a measurement device (Charlie; C) in between them. Charlie performs a BSM and announces the result. After verifying in which rounds Alice and Bob sent qubits in compatible bases, a sifted key is generated. **b**, Illustration of memory-enhanced protocol. Photons arrive at Charlie from A and B at random times over a lossy channel, and are unlikely to arrive simultaneously (rare success indicated in purple), leading to a low BSM success rate for direct transmission. Despite overhead time T_R associated with operating a quantum memory (red), a BSM can be performed between photons that arrive at Charlie within memory coherence time T_2, leading to higher success rates (green). BSM successes and failures are denoted by dark and light shaded windows respectively for both approaches.

and adiabatically transferred into a single-mode optical fibre[18] that is routed to superconducting nanowire single-photon detectors, yielding a full system detection efficiency of about 85% (Methods). The device is placed inside a dilution refrigerator, resulting in an electronic spin quantum memory[19] time $T_2 > 0.2$ ms at temperatures below 300 mK.

The operating principle of the SiV–cavity-based spin–photon interface is illustrated in Fig. 2. Spin-dependent modulation of the cavity reflection at incident probe frequency f_0 (Fig. 2b) results in the direct observation of electron spin quantum jumps (Fig. 2c, inset), enabling non-destructive single-shot readout of the spin state (Fig. 2c) in 30 μs with fidelity $F = 0.9998^{+0.0002}_{-0.0003}$. Coherent control of the SiV spin qubit ($f_Q \approx 12$ GHz) is accomplished using microwave fields delivered via an on-chip gold coplanar waveguide[19]. We utilize both optical readout and microwave control to perform projective feedback-based initialization of the SiV spin into the $|\downarrow\rangle$ state with a fidelity of $F = 0.998 \pm 0.001$. Spin-dependent cavity reflection also enables quantum logic operations between an incoming photonic time-bin qubit, defined by a phase-coherent pair of attenuated laser pulses, and the spin memory[19,29]. We characterize this by using the protocol illustrated in Fig. 2d to generate the spin–photon entangled state $(|e\uparrow\rangle + |l\downarrow\rangle)/\sqrt{2}$ conditioned on successful reflection of an incoming single photon with overall heralding efficiency $\eta = 0.423 \pm 0.004$ (Methods). Here, $|e\rangle$ and $|l\rangle$ denote respectively the presence of a photon in an early or a late time-bin, separated by $\delta t = 142$ ns. We characterize the entangled state by performing measurements in the joint spin–photon ZZ and XX bases (Fig. 2e), implementing local operations on the reflected photonic qubit with a time-delay interferometer (TDI; Fig. 2a, dashed box). By lowering the average number of photons $\langle n\rangle_m$ incident on the device during the SiV memory time, we reduce the possibility that an additional photon reaches the cavity without being subsequently detected, enabling high spin–photon gate fidelities for small $\langle n\rangle_m$ (Fig. 2f). For $\langle n\rangle_m = 0.002$ we measure a lower bound on the fidelity[19] of the spin–photon entangled state of $F \geq 0.944 \pm 0.008$, primarily limited by residual reflections from the $|\downarrow\rangle$ state.

Asynchronous BSMs

This spin–photon logic gate can be directly used to herald the storage of an incoming photonic qubit by interferometrically measuring the reflected photon in the X basis[19]. To implement a memory-assisted BSM, we extend this protocol to accommodate a total of N photonic qubit time-bins within a single initialization of the memory (Fig. 3a). Each individual time-bin qubit is encoded in the relative amplitudes and phases of a pair of neighbouring pulses separated by δt. Detection of a reflected photon heralds the arrival of the photonic qubit formed by the two interfering pulses without revealing its state[19]. Two such heralding events, combined with subsequent spin-state readout in the X basis, constitute a successful BSM on the incident photons. This can be understood without loss of generality by restricting input photonic states to be encoded in the relative phase ϕ between neighbouring pulses with equal amplitude: $(|e\rangle + e^{i\phi}|l\rangle)/\sqrt{2}$ (Fig. 3b). Detection of the first reflected photon in the X basis teleports its quantum state onto the spin, resulting in the state $(|\uparrow\rangle + m_1 e^{i\phi_1}|\downarrow\rangle)/\sqrt{2}$, where $m_1 = \pm 1$ depending on which detector registers the photon[19]. Detection of a second photon at a later time within the electron spin T_2 results in the spin state $(|\uparrow\rangle + m_1 m_2 e^{i(\phi_1+\phi_2)}|\downarrow\rangle)/\sqrt{2}$. The phase of this spin state depends only on the sum of the incoming phases and the product of their detection outcomes, but not the individual phases themselves. As a result, if the photons were sent with phases that meet the condition $\phi_1 + \phi_2 \in \{0, \pi\}$, a final measurement of the spin in the X basis ($m_3 = \pm 1$) completes an asynchronous BSM, distinguishing two of the four Bell states based on the total parity $m_1 m_2 m_3 = \pm 1$ (Supplementary Information, Extended Data Table 3).

This approach can be directly applied to generate a correlated bit-string within the protocol illustrated in Fig. 1a. We analyse the system performance by characterizing the overall quantum-bit error rate (QBER)[4,22] for $N = 124$ photonic qubits per memory initialization. We use several random bit strings of incoming photons from $\{|\pm x\rangle, |\pm y\rangle\}$ and observe strong correlations between the resulting BSM outcome and the initial combination of input qubits for both bases (Fig. 3c). Using this method, we estimate the average QBER to be $E = 0.116 \pm 0.002$ for all combinations of random bit strings measured, significantly ($P < 10^{-20}$) below the limit of $E_{ia} = 0.146$, which could provide security against individual attacks[4] (note that the measured error rate is also well below the minimum average QBER[22] of $E_{lo} = 0.125$ achievable using a linear optics BSM with weak coherent pulse inputs, see Supplementary Information). In our experiment, the QBER is affected by technical imperfections in the preparation of random strings of photonic qubits. We find specific periodic patterns of photonic qubits to be less prone to these effects, resulting in a QBER as low as $E = 0.097 \pm 0.006$, which falls within the threshold corresponding to unconditional security[3] of $E_u = 0.110$ with a confidence level of 0.986 (Supplementary Information). We further verify security by testing the Bell-CHSH inequality[14]

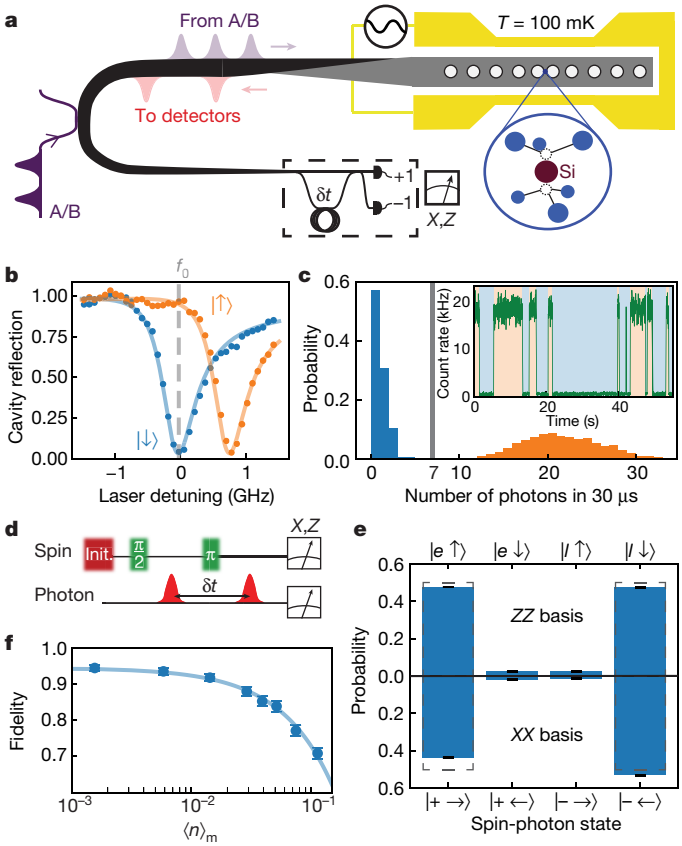

Fig. 2 | Realization of heralded spin–photon gate. a, Schematic of memory-assisted implementation of Charlie's measurement device, consisting of a diamond nanophotonic resonator (grey) containing SiV quantum memory (blue circle) with an integrated microwave stripline (yellow). Weak pulses derived from a single laser simulate incoming photons from Alice and Bob (purple). Reflected photons (red) are detected in a heralding set-up (dashed box). **b**, Reflection spectrum of the memory node, showing spin-dependent device reflectivity. **c**, Histogram of detected photon numbers during a 30-μs laser pulse, enabling single-shot readout based on a threshold of 7 photons. Inset, electron spin quantum jumps under weak illumination. **d**, Schematic of spin–photon quantum logic operation used to generate and verify spin–photon entangled state. **e**, Characterization of resulting spin–photon correlations in the *ZZ* and *XX* bases. Dashed bars show ideal values. **f**, Measured spin–photon entanglement fidelity as a function of $\langle n\rangle_m$, the average incident photon number during each initialization of the memory. Error bars, 68% confidence interval (c.i.). See main text and Methods for details of nomenclature used in this figure.

using input states from four different bases, each separated by an angle of 45° (Supplementary Information). We find that the correlations between input photons (Fig. 3d) violate the Bell-CHSH inequality $S_{\pm} \leq 2$, observing $S_{+} = 2.21 \pm 0.04$ and $S_{-} = 2.19 \pm 0.04$ for positive and negative BSM parity results, respectively. This result demonstrates that this device can be used for quantum communication that is secured by Bell's theorem.

Benchmarking quantum memory advantage

To benchmark the performance of memory-assisted quantum communication, we model an effective channel loss by reducing the mean photon number $\langle n\rangle_p$ incident on the device per photonic qubit. Assuming that Alice and Bob emit roughly one photon per qubit, this yields an effective channel transmission probability $p_{A\to B} = \langle n\rangle_p^2$, resulting in the maximal distilled key rate R_{max} per channel use for the direct-transmission approach[22], given by the red line in Fig. 4. We emphasize that this is a theoretical upper bound for a linear-optics-based BSM, assuming ideal single-photon sources and detectors and balanced basis choices. The measured sifted key rates of the memory-based device are plotted as open circles in Fig. 4. Owing to the high overall heralding efficiency and the large number of photonic qubits per memory time (up to $N = 504$), the memory-assisted sifted key rate exceeds the capability of a linear-optics-based BSM device by a factor of 78.4 ± 0.7 at an effective channel loss of about 88 dB.

In practice, errors introduced by the quantum memory node could leak information to the environment, reducing the quality and potential security of the sifted key[3]. A shorter secure key can be recovered from a sifted key with finite QBER using classical error correction and privacy amplification techniques. The fraction of distilled bits r_s that can be secure against individual attacks rapidly diminishes[4] as the QBER approaches $E_{ia} = 0.147$. For each value of the effective channel loss, we estimate the QBER and use it to compute r_s, enabling extraction of distilled key rates R_S, plotted in black in Fig. 4. Even after error correction, we find that the memory-assisted distilled key rate outperforms the ideal limit for the corresponding direct-transmission implementation by a factor of up to $R_S/R_{max} = 4.1 \pm 0.5$ (± 0.1 systematic uncertainty, for $N = 124$). We further find that this rate also exceeds the fundamental bound on repeaterless communication[8] $R_S \leq 1.44 p_{A\to B}$ with a statistical confidence level of 99.2% (with $^{+0.2\%}_{-0.3\%}$ systematic uncertainty, see Methods). Despite experimental overhead time associated with operating the device (T_R in Fig. 1b), the performance of the memory-assisted BSM node (for $N = 248$) is competitive with an ideal unassisted system running at a 4 MHz average clock rate (Methods).

Outlook

These experiments demonstrate a form of quantum advantage allowed by memory-based communication nodes and represent a crucial step towards realizing functional quantum repeaters. Several important

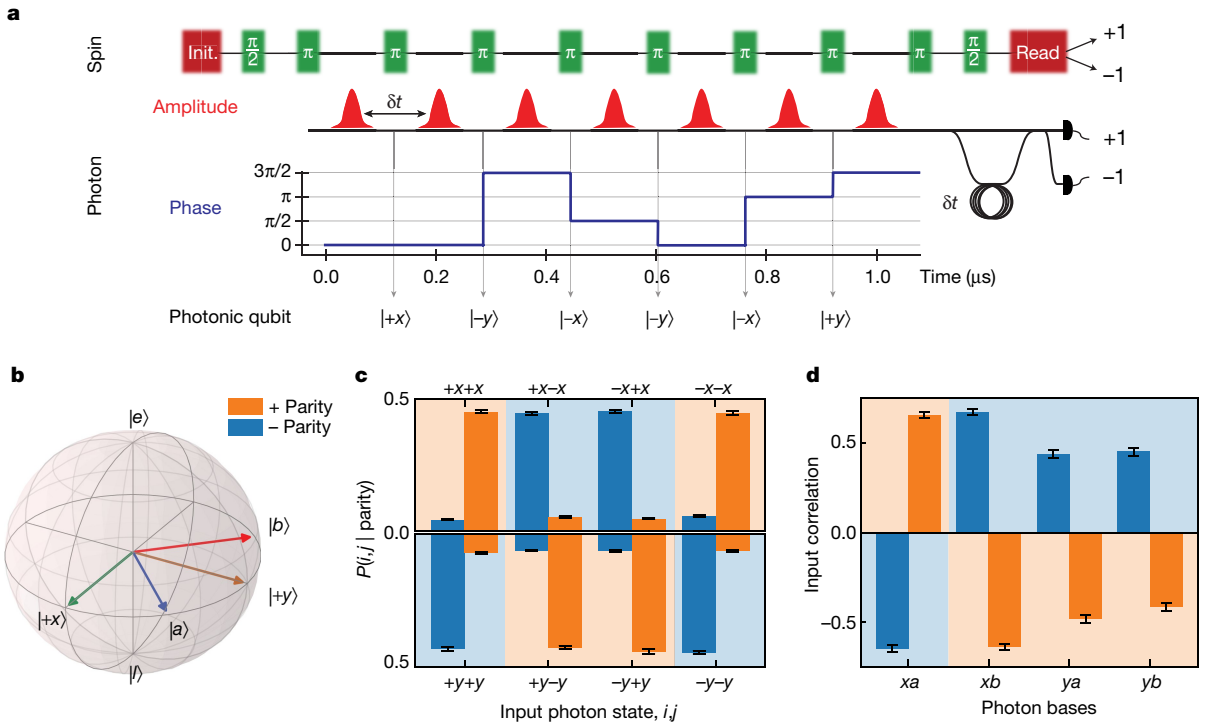

Fig. 3 | Asynchronous BSMs using quantum memory. a, Example sequence with $N = 6$ photonic qubits sent in a single memory time. Microwave π pulses (green) are interleaved with incoming optical pulses. Photons have fixed amplitude (red) and qubits are defined by the relative phases between subsequent pulses (blue). **b**, Bloch sphere representation of input photonic time-bin qubits used for characterization. **c**, Characterization of asynchronous BSM. Shown are conditional probabilities for Alice and Bob to have sent input states (i,j) given a particular parity outcome for input states in the X (top) and Y (bottom) bases. **d**, Bell test using the CHSH inequality. Conditioned on the BSM outcome, the average correlation between input photons is plotted for each pair of bases used (Supplementary Information). Shaded backgrounds denote the expected parity. Error bars, 68% c.i. See main text for details.

technical improvements will be necessary to apply this advance to practical long-distance quantum communication. First, this protocol must be implemented using truly independent, distant communicating parties. Second, frequency conversion from telecommunications wavelengths to 737 nm, as well as low-loss optical elements used for routeing photons to and from the memory node, will need to be incorporated. Last, rapid generation of provably secure keys will require implementation of decoy-state protocols[26], biased bases[27] and finite-key error analyses[28], all compatible with the present approach. With these improvements, our approach is well-suited for deployment in real-world settings. It does not require phase stabilization of long-distance links and operates efficiently in the relevant regime of $p_{A\to B} \approx 70$ dB, corresponding to about 350 km of telecommunications fibre. Additionally, a single device can be used at the centre of a star network topology[30], enabling quantum communication between several parties beyond the metropolitan scale.

Furthermore, the present approach could be extended along several directions. The use of long-lived ^{13}C nuclear spin qubits could eliminate the need to operate at low total $\langle n\rangle_m$ and would provide longer storage times, potentially enabling 100-fold enhancement of BSM success rates[15,19]. Recently implemented strain-tuning capabilities[31] should allow for operation of many quantum nodes at a common network frequency. Also, unlike linear-optics-based alternatives[24], the approach presented here could be extended to implement the full repeater protocol, enabling a polynomial scaling of the communication rate with distance[9]. Last, the demonstrated multi-photon gate operations could also be adapted to engineer large cluster-states of entangled photons[32], which can be used for rapid quantum communication[33]. Implementation of these techniques could enable the realization and application of scalable quantum networks[1] beyond quantum key distribution, ranging from non-local quantum metrology[20] to modular quantum computing architectures[21].

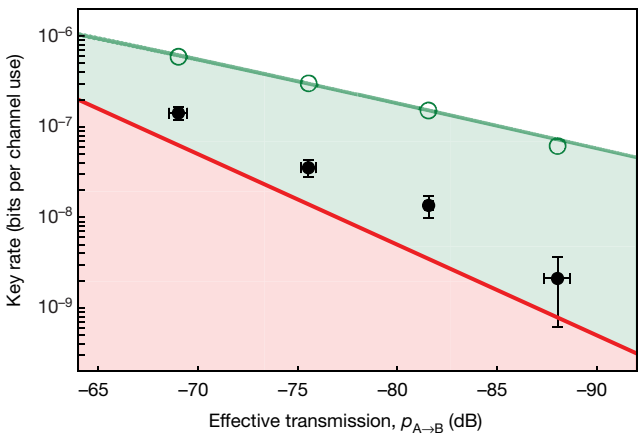

Fig. 4 | Performance of memory-assisted quantum communication. Shown is a log–log plot of key rate in bits per channel use versus effective channel transmission ($p_{A\to B} = \langle n\rangle_p^2$, where $\langle n\rangle_p$ is the average number of photons incident on the measurement device per photonic qubit). Red line, theoretical maximum for loss-equivalent direct-transmission experiment. Green open circles, experimentally measured sifted key rate (green line is the expected rate). To ensure optimal operation of the memory, $\langle n\rangle_m = \langle n\rangle_p N \approx 0.02$ is kept constant (Methods). From left to right, points correspond to $N = \{60, 124, 248, 504\}$. Black filled circles, distilled key rates R_s using memory device. Vertical error bars, 68% c.i.; horizontal error bars, s.d. of the systematic power fluctuations.

Online content

Any methods, additional references, Nature Research reporting summaries, source data, extended data, supplementary information, acknowledgements, peer review information; details of author contributions and competing interests; and statements of data and code availability are available at https://doi.org/10.1038/s41586-020-2103-5.

1. Kimble, H. J. The quantum internet. *Nature* **453**, 1023–1030 (2008).
2. Bennett, C. H. & Brassard, G. Quantum cryptography: public key distribution and coin tossing. In *Proc. Int. Conf. on Computers, Systems and Signal Processing* Vol. 1, 175–179 (IEEE Computer Society, IEEE Circuits and Systems Society, Indian Institute of Science, 1984).
3. Shor, P. W. & Preskill, J. Simple proof of security of the BB84 quantum key distribution protocol. *Phys. Rev. Lett*. **85**, 441–444 (2000).
4. Gisin, N., Ribordy, G., Tittel, W. & Zbinden, H. Quantum cryptography. *Rev. Mod. Phys*. **74**, 145–195 (2002).
5. Boaron, A. et al. Secure quantum key distribution over 421 km of optical fiber. *Phys. Rev. Lett*. **121**, 190502 (2018).
6. Zhang, Q., Xu, F., Chen, Y.-A., Peng, C.-Z. & Pan, J.-W. Large scale quantum key distribution: challenges and solutions. *Opt. Express* **26**, 24260–24273 (2018).
7. Pirandola, S. et al. Advances in quantum cryptography. Preprint at http://arxiv.org/abs/1906.01645 (2019).
8. Pirandola, S., Laurenza, R., Ottaviani, C. & Banchi, L. Fundamental limits of repeaterless quantum communications. *Nat. Commun*. **8**, 15043 (2017).
9. Briegel, H.-J., Dür, W., Cirac, J. I. & Zoller, P. Quantum repeaters: the role of imperfect local operations in quantum communication. *Phys. Rev. Lett*. **81**, 5932–5935 (1998).
10. Chou, C.-W. et al. Functional quantum nodes for entanglement distribution over scalable quantum networks. *Science* **316**, 1316–1320 (2007).
11. Yuan, Z.-S. et al. Experimental demonstration of a BDCZ quantum repeater node. *Nature* **454**, 1098–1101 (2008).
12. Gao, W. B., Fallahi, P., Togan, E., Miguel-Sanchez, J. & Imamoglu, A. Observation of entanglement between a quantum dot spin and a single photon. *Nature* **491**, 426–430(2012).
13. Reiserer, A. & Rempe, G. Cavity-based quantum networks with single atoms and optical photons. *Rev. Mod. Phys*. **87**, 1379–1418 (2015).
14. Hensen, B. et al. Loophole-free Bell inequality violation using electron spins separated by 1.3 kilometres. *Nature* **526**, 682–686 (2015).
15. Kalb, N. et al. Entanglement distillation between solid-state quantum network nodes. *Science* **356**, 928–932 (2017).
16. Kaneda, F., Xu, F., Chapman, J. & Kwiat, P. G. Quantum-memory-assisted multi-photon generation for efficient quantum information processing. *Optica* **4**, 1034–1037 (2017).
17. Evans, R. E. et al. Photon-mediated interactions between quantum emitters in a diamond nanocavity. *Science* **362**, 662–665 (2018).
18. Burek, M. J. et al. Fiber-coupled diamond quantum nanophotonic interface. *Phys. Rev. Appl*. **8**, 024026 (2017).
19. Nguyen, C. T. et al. Quantum network nodes based on diamond qubits with an efficient nanophotonic interface. *Phys. Rev. Lett*. **123**, 183602 (2019).
20. Khabiboulline, E. T., Borregaard, J., De Greve, K. & Lukin, M. D. Optical interferometry with quantum networks. *Phys. Rev. Lett*. **123**, 070504 (2019).
21. Monroe, C. et al. Large-scale modular quantum-computer architecture with atomic memory and photonic interconnects. *Phys. Rev. A* **89**, 022317 (2014).
22. Lo, H.-K., Curty, M. & Qi, B. Measurement-device-independent quantum key distribution. *Phys. Rev. Lett*. **108**, 130503 (2012).
23. Braunstein, S. L. & Pirandola, S. Side-channel-free quantum key distribution. *Phys. Rev. Lett*. **108**, 130502 (2012).
24. Minder, M. et al. Experimental quantum key distribution beyond the repeaterless secret key capacity. *Nat. Photon*. **13**, 334–338 (2019).
25. Panayi, C., Razavi, M., Ma, X. & Lütkenhaus, N. Memory-assisted measurement-device-independent quantum key distribution. *New J. Phys*. **16**, 043005 (2014).
26. Lo, H.-K., Ma, X. & Chen, K. Decoy state quantum key distribution. *Phys. Rev. Lett*. **94**, 230504 (2005).
27. Lo, H.-K., Chau, H. F. & Ardehali, M. Efficient quantum key distribution scheme and a proof of its unconditional security. *J. Cryptol*. **18**, 133–165 (2005).
28. Curty, M. et al. Finite-key analysis for measurement-device-independent quantum key distribution. *Nat. Commun*. **5**, 3732 (2014).
29. Duan, L.-M. & Kimble, H. J. Scalable photonic quantum computation through cavity-assisted interactions. *Phys. Rev. Lett*. **92**, 127902 (2004).
30. Biham, E., Huttner, B. & Mor, T. Quantum cryptographic network based on quantum memories. *Phys. Rev. A* **54**, 2651–2658 (1996).
31. Machielse, B. et al. Quantum interference of electromechanically stabilized emitters in nanophotonic devices. *Phys. Rev. X* **9**, 031022 (2019).
32. Raussendorf, R. & Briegel, H. J. A one-way quantum computer. *Phys. Rev. Lett*. **86**, 5188–5191 (2001).
33. Borregaard, J. et al. One-way quantum repeater based on near-deterministic photon-emitter interfaces. Preprint at http://arxiv.org/abs/1907.05101 (2019).

Methods

Experimental set-up

We perform all measurements in a dilution refrigerator (BlueFors BF-LD250) with a base temperature of 20 mK. The dilution refrigerator is equipped with a superconducting vector magnet (American Magnets Inc. 6-1-1 T), a home-built free-space wide-field microscope with a cryogenic objective (Attocube LT-APO-VISIR), piezo positioners (Attocube ANPx101 and ANPx311 series), and fibre and microwave feedthroughs. Tuning of the nanocavity resonance is performed using a gas condensation technique[17]. The SiV–cavity system is optically interrogated through the fibre network without any free-space optics[19]. The operating temperature of the memory node during the BSM measurements was 100–300 mK. We note that similar performance at higher temperatures should be feasible in future experiments by using recent developments with heavier group-IV colour centres[34] or highly strained SiV centres[35]. Additional details about the experimental set-up and device fabrication[18,31,36,37] for millikelvin nanophotonic cavity quantum electrodynamic experiments with SiV centres are thoroughly described elsewhere[38].

Nanophotonic quantum memory

A spectrum of the SiV–cavity system at large detuning (248 GHz) allows us to measure the cavity linewidth $\kappa = 21.6 \pm 1.3$ GHz (Extended Data Fig. 2a, blue curve) and natural SiV linewidth $\gamma = 0.123 \pm 0.010$ GHz (Extended Data Fig. 2a, red curve). We find spectral diffusion of the SiV optical frequency to be much smaller than γ on minute timescales with an excitation photon flux of less than 1 MHz. Next, we estimate the single-photon Rabi frequency, g, using the cavity reflection spectrum for zero atom–cavity detuning, shown in red in Extended Data Fig. 2a. For a resonant atom–cavity system probed in reflection from a single port with cavity–waveguide coupling κ_{wg}, the cavity reflection coefficient[13] as a function of probe detuning Δ_c is given by

$$r(\Delta_c) = \frac{i\Delta_c + \frac{g^2}{i\Delta_c + \frac{\gamma}{2}} - \kappa_{wg} + \frac{\kappa}{2}}{i\Delta_c + \frac{g^2}{i\Delta_c + \frac{\gamma}{2}} + \frac{\kappa}{2}} \quad (1)$$

By fitting $|r(\Delta_c)|^2$ using known values of κ and γ, we obtain the solid red curve in Extended Data Fig. 2a, which corresponds to a single-photon Rabi frequency $g = 8.38 \pm 0.05$ GHz, yielding the estimated cooperativity $C = \frac{4g^2}{\kappa\gamma} = 105 \pm 11$.

Microwave control

We use resonant microwave pulses delivered via an on-chip coplanar waveguide to coherently control the quantum memory[19,38]. We measure the spectrum of the spin-qubit transition by applying a weak, 10-μs-long microwave pulse of variable frequency, observing the optically detected magnetic resonance spectrum presented in Extended Data Fig. 3a. We note that the spin-qubit transition is split by the presence of a nearby ^{13}C. While coherent control techniques can be employed to use the ^{13}C as an additional qubit[19,38], we do not control or initialize it in this experiment. Instead, we drive the electron spin with strong microwave pulses at a frequency f_Q such that both ^{13}C-state-specific transitions are addressed equally. This also mitigates slow spectral diffusion of the microwave transition[38] of ~100 kHz.

After fixing the microwave frequency at f_Q, we vary the length of this drive pulse (τ_R in Extended Data Fig. 3b) and observe full-contrast Rabi oscillations. We choose a π time of 32 ns in the experiments in the main text, which is a compromise between two factors: (1) it is sufficiently fast such that we can temporally multiplex between 2 and 4 time-bin qubits around each microwave π pulse and (2) it is sufficiently weak to minimize heating-related effects from high microwave currents in resistive gold coplanar waveguide.

With known π time, we measure the coherence time of the SiV spin qubit under an XY8-1 dynamical decoupling sequence to exceed 200 μs (Extended Data Fig. 3c). In the main experiment we use decoupling sequences with more π pulses. As an example, Extended Data Fig. 3d shows the population in the $|\uparrow\rangle$ state after the XY8-8 decoupling sequence (total $N_\pi = 64$ π pulses) as a function of τ, half of the inter-pulse spacing. For BSM experiments, this inter-pulse spacing, 2τ, is fixed and is matched to the time-bin interval δt. While at some times (for example, $\tau = 64.5$ ns) there is a loss of coherence due to entanglement with the nearby ^{13}C, at $2\tau = 142$ ns we are decoupled from this ^{13}C and can maintain a high degree of spin coherence. Thus we chose the time-bin spacing to be 142 ns. The spin coherence at $2\tau = 142$ ns is plotted as a function of N_π in Extended Data Fig. 3e, and decreases for large N_π, primarily owing to heating-related effects[19].

Fibre network

The schematic of the fibre network used to deliver optical pulses to and collect reflected photons from the nanophotonic memory device is shown in Extended Data Fig. 1b. Photons are routed through the lossy (1%) port of a 99:1 fibre beamsplitter to the nanophotonic device. We note that for practical implementation of memory-assisted quantum communication, an efficient optical switch or circulator should be used instead. In this experiment, since we focus on benchmarking the performance of the memory device itself, the loss introduced by this beamsplitter is incorporated into the estimated channel loss. Reflected photons are collected and routed back through the efficient (99%) port of the fibre beamsplitter and are sent to the TDI in the heralding set-up. The outputs of the TDI are sent back into the dilution refrigerator and directly coupled to superconducting nanowire single photon detectors (SNSPDs, PhotonSpot), which are mounted at the 1 kelvin plate of the dilution refrigerator and are coated with dielectrics to optimize detection efficiency exactly at 737 nm.

The total heralding efficiency η of the memory node is an important parameter since it directly affects the performance of the BSM for quantum communication experiments. One of the contributing factors is the detection quantum efficiency (QE) of the fibre-coupled SNSPDs. To estimate it, we compare the performance of the SNSPDs to the specifications of calibrated conventional avalanche photodiode single-photon counters (Laser Components COUNT-10C-FC). The estimated QEs of the SNSPDs with this method are as close to unity as we can verify. Additionally, we measure <1% reflection from the fibre–SNSPD interface, which typically is the dominant contribution to the reduction of QE in these devices. Thus we assume the lower bound of the QE of the SNSPDs to be $\eta_{QE} = 0.99$ for the rest of this section. Of course, this estimation is subject to additional systematic errors. However, the actual QE of these detectors would be a common factor (and thus drop out) in a comparison between any two physical quantum communication systems.

Here we use two different approaches to estimate η. We first measure the most dominant loss, which arises from the average reflectivity of the critically coupled nanophotonic cavity (Fig. 2b). While the $|\uparrow\rangle$ state is highly reflecting (94.4%), the $|\downarrow\rangle$ state reflects only 4.1% of incident photons, leading to an average device reflectivity of $\eta_{sp} = 0.493$.

In method (1), we compare the input power photodiode M1 with that of photodiode MC (Extended Data Fig. 1b). This estimates a lower bound on the tapered-fibre diamond waveguide coupling efficiency of $\eta_c = 0.930 \pm 0.017$. This error bar arises from uncertainty due to photodiode noise and does not include systematic photodiode calibration uncertainty. However, we note that if the tapered fibre is replaced by a silver-coated fibre-based retroreflector, this calibration technique extracts a coupling efficiency of $\eta_c^{cal} \approx 0.98$, which is consistent with the expected reflectivity from such a retroreflector. We independently calibrate the efficiency through the 99:1 fibre beamsplitter and the TDI to be $\eta_f = 0.934$. This gives us our first estimate on the overall heralding efficiency $\eta = \eta_{sp}\eta_c\eta_f\eta_{QE} = 0.425 \pm 0.008$.

In method (2), during the experiment we compare the reflected counts from the highly reflecting ($|\uparrow\rangle$) spin-state measured on the SNSPDs with the counts on an avalanche photodiode single photon counting module (M2 in Extended Data Fig. 1b) which has a calibrated efficiency of ~0.7 relative to the SNSPDs. From this measurement, we estimate an overall efficiency of fibre–diamond coupling, as well as transmission through all relevant splices and beamsplitters, of $\eta_c\eta_f = 0.864 \pm 0.010$. This error bar arises from shot noise on the single photon detectors. Overall, this gives us a consistent estimate of $\eta = \eta_{sp}\eta_c\eta_f\eta_{QE} = 0.422 \pm 0.005$. Methods (1) and (2), which each have independent systematic uncertainties associated with imperfect photodetector calibrations, are consistent to within a small residual systematic uncertainty, which is noted in the text where appropriate.

Quantum communication experiment

An asynchronous BSM (Fig. 3a) relies on (1) precise timing of the arrival of optical pulses (corresponding to photonic qubits[39,40] from Alice and Bob) with microwave control pulses on the quantum memory, and (2) interferometrically stable rotations on reflected time-bin qubits for successful heralding, described in Extended Data Fig. 4.

In order to accomplish (1), all equipment used for generation of microwave and optical fields is synchronized by a single device (National Instruments HSDIO, Extended Data Fig. 1a) with programming described in Extended Data Tables 1, 2.

In order to accomplish (2), we use a single, narrow linewidth (<50 kHz) Ti:sapphire laser (M Squared SolsTiS-2000-PSX-XF, Extended Data Fig. 1b) both for generating photonic qubits and locking the TDI used to herald their arrival. In the experiment, photonic qubits are reflected from the device, sent into the TDI, and detected on the SNSPDs. All detected photons are processed digitally on a field-programmable gate array (FPGA, Extended Data Fig. 1a), and the arrival times of these heralding signals are recorded on a time-tagger (TT, Extended Data Fig. 1a), and constitute one bit of information of the BSM (m_1 or m_2). At the end of the experiment, a 30-μs pulse from the readout path is reflected off the device, and photons are counted in order to determine the spin state (m_3) depending on the threshold shown in Fig. 2c.

To minimize thermal drift of the TDI, it is mounted on a thermally weighted aluminium breadboard, placed in a polyurethane-foam-lined and sand-filled briefcase, and secured with glue to ensure passive stability on the minute timescale. We halt the experiment and actively lock the interferometer to the sensitive Y-quadrature every ~200 ms by changing the length of the roughly 28-m-long (142 ns) delay line with a cylindrical piezo. In order to use the TDI for X-measurements of the reflected qubits, we apply a frequency shift of 1.8 MHz using the qubit AOM, which is 1/4 of the free-spectral range of the TDI. Since the nanophotonic cavity, the TDI and the SNSPDs are all polarization sensitive, we use various fibre-based polarization controllers (Extended Data Fig. 1b). All fibres in the network are covered with aluminium foil to prevent thermal polarization drifts. This results in an interference visibility of the TDI of >99% that is stable for several days without any intervention with laboratory temperature and humidity variations of ±1 °C and ±5%, respectively.

In order to achieve high-fidelity operations, we have to ensure that the laser frequency (which is not locked) is resonant with the SiV frequency f_0 (which is subject to the spectral diffusion[38]). To do that, we implement a so-called preselection procedure, described in Extended Data Tables 1, 2 and Extended Data Fig. 1a. First, the SiV spin state is initialized by performing a projective measurement and applying microwave feedback. During each projective readout, the reflected counts are compared with two thresholds: a 'readout' threshold of 7 photons (used only to record m_3), and a 'status' threshold of 3 photons. The status trigger is used to prevent the experiment from running in cases when the laser is no longer on resonance with f_0, or if the SiV has ionized to an optically inactive charge state. The duty cycle of the status trigger is externally monitored, and is used to temporarily abort the experiment and run an automated re-lock procedure that locates and sets the laser to the new frequency f_0, reinitializing the SiV charge state with a 520 nm laser pulse if necessary. This protocol enables fully automated operation at high fidelities (low QBER) for several days without human intervention.

Optimal parameters for asynchronous BSMs

We minimize the experimentally extracted QBER for the asynchronous BSM to optimize the performance of the memory node. One major factor contributing to QBER is the scattering of a third photon that is not detected, owing to the finite heralding efficiency $\eta = 0.423 \pm 0.04$. This is shown in Fig. 2f, where the fidelity of the spin–photon entangled state diminishes for $\langle n\rangle_m \gtrsim 0.02$. At the same time, we would like to work at the maximum possible $\langle n\rangle_m$ in order to maximize the data rate to get enough statistics to extract QBER (and in the quantum communication setting, efficiently generate a key).

To increase the key generation rate per channel use, one can also fit many photonic qubits within each initialization of the memory. In practice, there are two physical constraints: (1) the bandwidth of the SiV–photon interface; and (2) the coherence time of the memory. We find that one can satisfy (1) at a bandwidth of roughly 50 MHz with no measurable infidelity. For shorter optical pulses (<10 ns), the spin–photon gate fidelity is reduced. In principle, the SiV–photon bandwidth can be increased by reducing the atom–cavity detuning (here ~60 GHz) at the expense of having to operate at higher magnetic fields where microwave qubit manipulation is not as convenient[38].

Even with just an XY8-1 decoupling sequence (number of π pulses $N_\pi = 8$), the coherence time of the SiV is longer than 200 μs (Extended Data Fig. 3c) and can be prolonged to the millisecond range with longer pulse sequences[19]. Unfortunately, to satisfy the bandwidth criterion (1) above, and to drive both hyperfine transitions (Extended Data Fig. 3a), we must use short (32-ns-long) π pulses, which already cause additional decoherence from ohmic heating[38] at $N_\pi = 64$ (Extended Data Fig. 3e). Because of this, we limit the pulse sequences to a maximum $N_\pi = 128$, and only use up to ~20 μs of the memory time. One solution would be to switch to superconducting microwave delivery. Alternatively, we could use a larger value of τ to allow the device to cool down between pulses[38] at the expense of having to stabilize a TDI of larger δt. Working at larger δt would also enable temporal multiplexing by fitting multiple time-bin qubits per free-precession interval. In fact, with $2\tau = 142$ ns, even given constraint (1) and the finite π time, we can fit up to 4 optical pulses per free-precession window, enabling a total number of photonic qubits of up to $N = 504$ for an N_π of only 128.

In benchmarking the asynchronous BSM for quantum communication, we optimize the parameters $\langle n\rangle_m$ and N to maximize our enhancement over the direct-transmission approach. The enhancement is a combination of both increasing N and reducing the QBER, since a large QBER results in a small distilled key fraction r_s. As described in the main text, the effective loss can be associated with $\langle n\rangle_p$, which is the average number of photons per photonic qubit arriving at the device, and is given straightforwardly by $\langle n\rangle_p = \langle n\rangle_m/N$. The most straightforward way to sweep the loss is to keep the experimental sequence the same (fixed N) and vary the overall power, which changes $\langle n\rangle_m$. The results of such a sweep are shown in Extended Data Fig. 5a, b. For larger $\langle n\rangle_m$ (corresponding to lower effective channel losses), the errors associated with scattering an additional photon reduce the performance of the memory device.

Owing to these considerations, we work at roughly $\langle n\rangle_m \lesssim 0.02$ for experiments reported in the main text and shown in Figs. 3 and 4, below which the performance does not improve substantially. At this value, we obtain BSM successes at a rate of roughly 0.1 Hz. By fixing $\langle n\rangle_m$ and increasing N, we maintain a tolerable BSM success rate while increasing the effective channel loss. Eventually, as demonstrated in Extended Data Fig. 5c and in the high-loss data point in Fig. 4, effects associated with microwave heating result in errors that again diminish the

performance of the memory node for large N. As such, we conclude that the optimal performance of our node occurs for $\langle n\rangle_m \approx 0.02$ and $N \approx 124$, corresponding to an effective channel loss of 69 dB between Alice and Bob, which is equivalent to roughly 350 km of telecommunications fibre.

We also find that the QBER and thus the performance of the communication link is limited by imperfect preparation of photonic qubits. Photonic qubits are defined by sending arbitrary phase patterns generated by the optical arbitrary waveform generator to a phase modulator. For an example of such a pattern, see the blue curve in Fig. 3a. We use an imperfect pulse amplifier with finite bandwidth (0.025–700 MHz), and find that the DC component of these waveforms can result in error in photonic qubit preparation at the few per cent level. By using a tailored waveform of phases with smaller (or vanishing) DC component, we can reduce these errors. We run such an experiment during the test of the Bell-CHSH inequality. We find that by evaluating BSM correlations from $|\pm a\rangle$ and $|\pm b\rangle$ inputs during this measurement, we estimate a QBER of 0.097 ± 0.006.

We obtain the effective clock-rate of the communication link by measuring the total number of photonic qubits sent over the course of an entire experiment. In practice, we record the number of channel uses, determined by the number of sync triggers recorded (see Extended Data Fig. 1a) as well as the number of qubits per sync trigger (N). We then divide this number by the total experimental time from start to finish (about 1–2 days for most experimental runs), including all experimental downtime used to stabilize the interferometer, read out and initialize the SiV, and compensate for spectral diffusion and ionization. For $N = 248$, we extract a clock rate of 1.2 MHz. As the distilled key rate in this configuration exceeds the conventional limit of $p/2$ by a factor of 3.8 ± 1.1, it is competitive with a standard linear-optics-based system operating at a $4.5^{+1.3}_{-1.2}$MHz clock rate.

Benchmarking memory-assisted operation

A single optical link can provide many channels—for example, by making use of different frequency, polarization or temporal modes. To account for this, when comparing different systems, data rates can be defined on a per-channel-use basis. In a quantum communication setting, full usage of the communication channel between Alice and Bob means that both links from Alice and Bob to Charlie are in use simultaneously. For an asynchronous sequential measurement, typically only half of the channel is used at a time, for example from Alice to Charlie or Bob to Charlie. The other half can in principle be used for a different task when not in use. For example, the unused part of the channel could be routed to a secondary asynchronous BSM device. In our experiment, we can additionally define as a second normalization the rate per channel 'occupancy', which accounts for the fact that only half the channel is used at any given time. The rate per channel occupancy is therefore half the rate per full channel use. For comparison, we typically operate at 1.2% channel use and 2.4% channel occupancy.

To characterize the optimal performance of the asynchronous Bell state measurement device, we operate it in the optimal regime determined above ($N = 124$, $\langle n\rangle_m \lesssim 0.02$). We note that the enhancement in the sifted key rate over direct transmission is given by

$$\frac{R}{R_{max}} = \eta^2 \frac{(N_\pi - 1)(N_\pi - 2)N_{sub}}{2N_\pi} \quad (2)$$

and is independent of $\langle n\rangle_m$ for a fixed number of microwave pulses (N_π) and optical pulses per microwave pulse (N_{sub}) and thus fixed $N = N_\pi N_{sub}$. For low $\langle n\rangle_m$, three photon events become negligible and therefore QBER saturates, such that the enhancement in the distilled key rate saturates as well (Extended Data Fig. 5a). We can therefore combine all data sets with fixed $N = 124$ below $\langle n\rangle_m \lesssim 0.02$ to characterize the average QBER of 0.116 ± 0.002 (Fig. 3c). The key rates cited in the main text relate to a data set in this series ($\langle n\rangle_m \approx 0.02$), with a QBER of 0.110 ± 0.004. A summary of key rates calculated on a per-channel use and per-channel occupancy basis, as well as comparisons of performance to an ideal linear-optics BSM and the repeaterless bound[8] are given in Extended Data Table 4.

Furthermore, we extrapolate the performance of our memory node to include biased input bases from Alice and Bob. This technique enables a reduction of channel uses where Alice and Bob send photons in different bases, but is still compatible with secure key distribution[27], allowing for distilled key rates enhanced by at most a factor of 2. The extrapolated performance of our node for a bias of 99:1 is also displayed in Extended Data Table 4, as well as comparisons to the relevant bounds. We note that basis biasing does not affect the performance when comparing to the equivalent direct-transmission experiment, which is limited by $p_{A\to B}/2$ in the unbiased case and $p_{A\to B}$ in the biased case. However, using biased input bases does make the performance of the memory-assisted approach more competitive with the fixed repeaterless bound[8] of $1.44p_{A\to B}$.

Data availability

All data related to the current study are available from the corresponding author on reasonable request.

34. Trusheim, M. E. et al. Lead-related quantum emitters in diamond. *Phys. Rev. B* **99**, 075430 (2019).
35. Meesala, S. et al. Strain engineering of the silicon-vacancy center in diamond. *Phys. Rev. B* **97**, 205444 (2018).
36. Burek, M. J. et al. High quality-factor optical nanocavities in bulk single-crystal diamond. *Nat. Commun.* **5**, 5718 (2014).
37. Atikian, H. A. et al. Freestanding nanostructures via reactive ion beam angled etching. *APL Photon.* **2**, 051301 (2017).
38. Nguyen, C. T. et al. An integrated nanophotonic quantum register based on silicon-vacancy spins in diamond. *Phys. Rev. B* **100**, 165428 (2019).
39. de Riedmatten, H. et al. Tailoring photonic entanglement in high-dimensional Hilbert spaces. *Phys. Rev. A* **69**, 050304 (2004).
40. Sasaki, T., Yamamoto, Y. & Koashi, M. Practical quantum key distribution protocol without monitoring signal disturbance. *Nature* **509**, 475 (2014).

Acknowledgements We thank P. Stroganov, K. de Greve, J. Borregaard, E. Bersin, B. Dixon, R. Murphy and N. Sinclair for discussions and experimental help, V. Anant from PhotonSpot for providing SNSPDs, and J. MacArthur for assistance with electronics. This work was supported by the NSF, CUA, DoD/ARO DURIP, AFOSR MURI, ONR MURI, ARL, DOE and a Vannevar Bush Faculty Fellowship. Devices were fabricated at Harvard CNS, NSF award no. 1541959. M.K.B. and D.S.L. acknowledge support from an NDSEG Fellowship. R.R. acknowledges support from the Alexander von Humboldt Foundation. B.M. and E.N.K. acknowledge support from an NSF GRFP.

Author contributions M.K.B., R.R., B.M., D.S.L., C.T.N., D.D.S. and M.D.L. planned the experiment, B.M. and E.N.K. fabricated the devices, M.K.B., R.R., B.M., D.S.L., C.T.N. and D.D.S. built the set-up, performed the experiment and analysed the data. All work was supervised by H.P., D.E., M.L. and M.D.L. All authors discussed the results and contributed to the manuscript. M.K.B., R.R., B.M., D.S.L. and C.T.N. contributed equally to this work.

Competing interests The authors declare no competing interests.

Additional information

Supplementary information is available for this paper at https://doi.org/10.1038/s41586-020-2103-5.

Correspondence and requests for materials should be addressed to M.D.L.

Peer review information *Nature* thanks Josh Nunn and Wolfgang Tittel for their contribution to the peer review of this work.

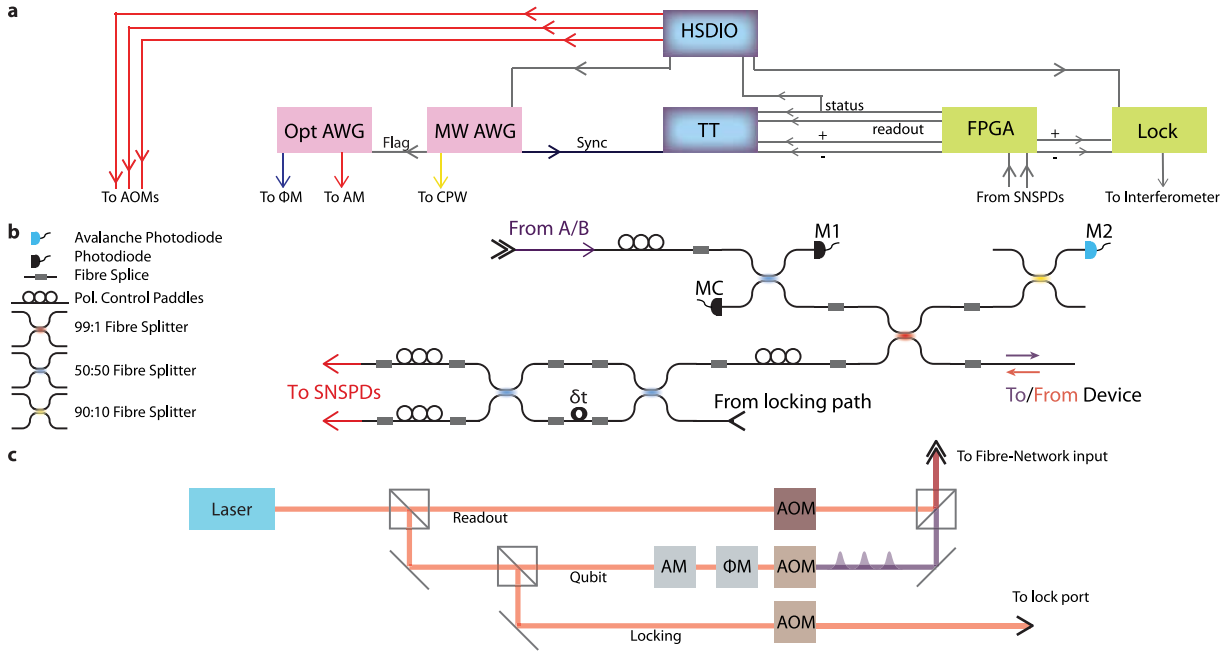

Extended Data Fig. 1 | Experimental schematic. a, Control flow of experiment. HSDIO (National Instruments) is a digital signal generator that synchronizes the experiment. Opt (MW) AWG is a Tektronix AWG7122B 5 GS/s (Tektronix AWG70001a 50 GS/s) arbitrary waveform generator used to generate photonic qubits (microwave control signals). All signals are recorded on a time-tagger (TT, PicoQuant HydraHarp 400). **b**, Fibre network used to deliver photons to and collect photons from the memory device, including elements for polarization control and diagnostic measurements of coupling efficiencies using photodiodes M1, M2 and MC. **c**, Preparation of optical fields. The desired phase relation between lock and qubit paths is ensured by modulating AOMs using phase-locked RF sources with a precise 1.8 MHz frequency shift between them. The AM (amplitude modulator) and ΦM (phase modulator) are used to define the photonic qubits.

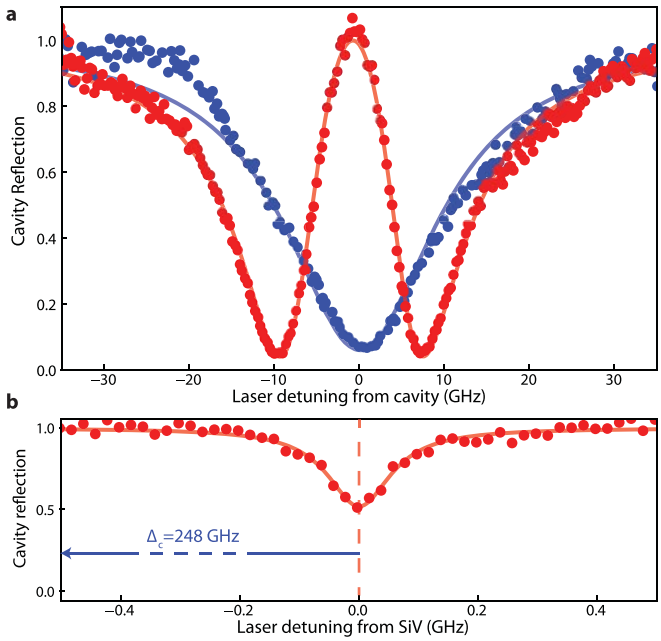

Extended Data Fig. 2 | Characterization of device cooperativity. a, Cavity reflection spectrum far-detuned (blue) and on resonance (red) with SiV centre. Blue solid line is a fit to a Lorentzian, enabling extraction of linewidth $\kappa = 21.8$ GHz. Red solid line is a fit to a model used to determine the single-photon Rabi frequency $g = 8.38 \pm 0.05$ GHz and shows the onset of a normal mode splitting. **b**, Measurement of SiV linewidth far detuned ($\Delta_c = 248$ GHz) from cavity resonance. Red solid line is a fit to a Lorentzian, enabling extraction of natural linewidth $\gamma = 0.123$ GHz.

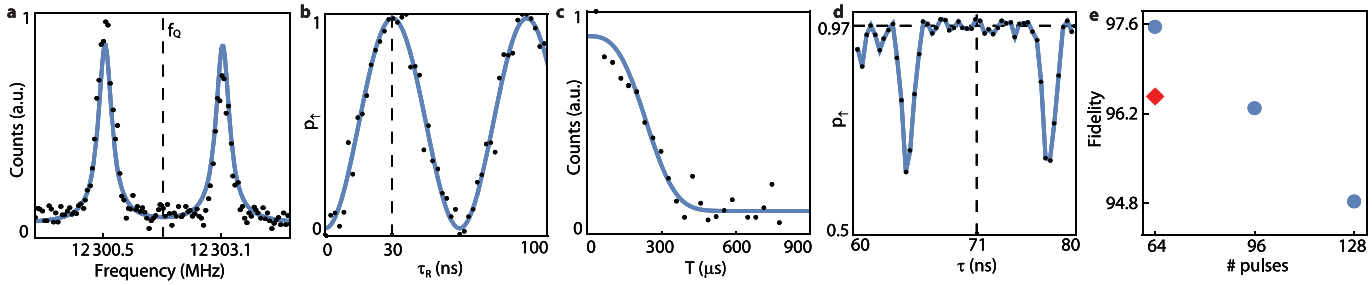

Extended Data Fig. 3 | Microwave characterization of spin-coherence properties. a, Optically detected magnetic resonance spectrum of the qubit transition at ~12 GHz split by coupling to a nearby ^{13}C. **b**, Rabi oscillations, read out via the population in the $|\uparrow\rangle$ state ($p_\uparrow$) showing π time of $\tau_R = 30$ ns. A π time of 32 ns is used for experiments reported in the main text. **c**, XY8-1 dynamical decoupling signal (unnormalized) as a function of total time T, showing coherence lasting on the timescale of several hundred microseconds. **d**, XY8-8 dynamical decoupling signal (normalized) revealing a region of high fidelity at the relevant value of $2\tau = 142$ ns. **e**, Fidelity of spin state after a dynamical decoupling sequence with varying numbers of π pulses (N_π; blue points). Red point (diamond) is under illumination with $\langle n \rangle_m = 0.02$.

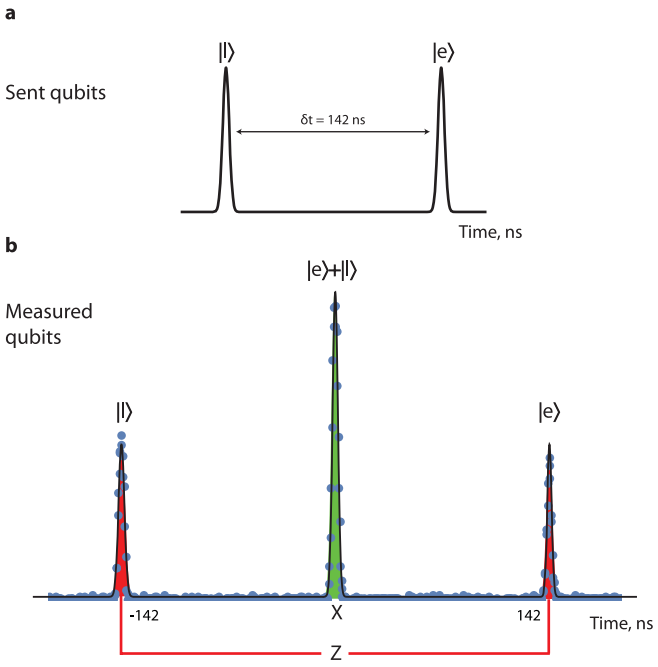

Extended Data Fig. 4 | Measurements on a single time-bin qubit in *Z* and *X* bases. a, Example of optical pulses sent in the experiment described in Fig. 2d. **b**, Time trace of detected photons on the + detector (see Fig. 2a) when the pulses shown in **a** are sent directly into the TDI. The first and last peaks correspond to late and early photons taking the long and short paths of the TDI, which enable measurements in the *Z* basis, $\{|e\rangle,|l\rangle\}$. The central bin corresponds to the late and early components overlapping and interfering constructively to come out of the + port, equivalent to a measurement of the time-bin qubit in the $|+x\rangle$ state. A detection event in this same timing window on the other detector (not shown) would constitute a $|-x\rangle$ measurement. In this measurement, the TDI was left unlocked, so we observe no interference in the central window.

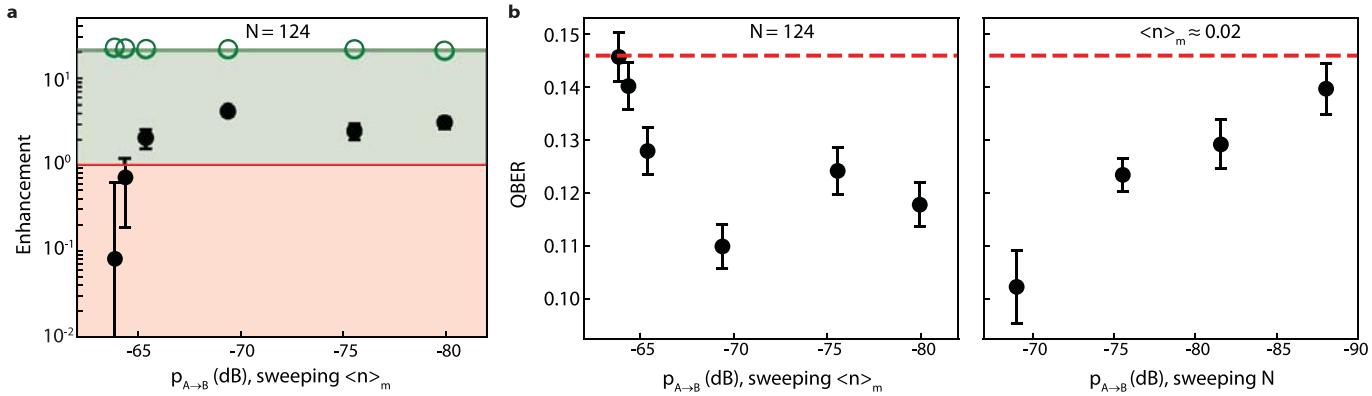

Extended Data Fig. 5 | Performance of memory device versus channel loss. a, Enhancement of memory-based approach compared to direct-transmission approach, keeping $N = 124$ fixed and varying $\langle n \rangle_m$ in order to vary the effective channel transmission probability, $p_{A\to B}$. At high $p_{A\to B}$ (larger $\langle n \rangle_m$), r_s approaches 0 owing to increased QBER arising from undetected scattering of a third photon. **b**, Left, plot of QBER for same sweep of $\langle n \rangle_m$ shown in **a**. Right, plot of QBER while sweeping N in order to vary loss. These points correspond to the same data shown in Fig. 4. At lower $p_{A\to B}$ (larger N), microwave-induced heating-related dephasing leads to increased QBER. Vertical error bars, 68% confidence interval; horizontal error bars, s.d. of the systematic power fluctuations.

Extended Data Table 1 | High-level experimental sequence

Step	Process	Duration	Proceed to
1	Lock time-delay interferometer	200 ms	2
2	Readout SiV	30 µs	If status LOW: 4, else: 3
3	Apply microwave π pulse	32 ns	2
4	Run main experiment script	$\sim$ 200 ms	1

This sequence (described by the 'Step' number, description of the 'Process', approximate 'Duration' and conditional step it 'Proceeds' to) is programmed into the HSDIO and uses feedback from the status trigger sent from the FPGA (see Extended Data Fig. 1a). The main experimental sequence is described in Extended Data Table 2. External software with a response time of 100 ms is also used to monitor the status trigger. If it is HIGH for $\gtrsim$2s, the software activates an automatic re-lock procedure which compensates for spectral diffusion and ionization of the SiV centre (Methods). Additionally, we keep track of the timing when the time-delay interferometer (TDI) piezo voltage reaches a limiting value. This guarantees that the SiV is always resonant with the photonic qubits and that the TDI performs high-fidelity measurements in the *X* basis.

Extended Data Table 2 | Main experimental sequence

Step	Process	Duration	Proceed to
1	Run sequence in Fig. 3a for a given N	$10 - 20$ µs	2
2	Readout SiV + report readout to TT	30 µs	If status LOW: 1, else: 3
3	Apply microwave π pulse	32 ns	4
4	Readout SiV	30 µs	If status LOW: 3, else: 1

This script is followed until step 1 is run a total of 4,000 times, and then terminates and returns to step 1 of Extended Data Table 1. The longest step is the readout step, which is limited by the fact that we operate at a photon detection rate of ~1 MHz to avoid saturation of the SNSPDs.

Extended Data Table 3 | Truth table of asynchronous BSM protocol

Alice	Bob	Parity	Bell state
$\|+x\rangle$	$\|+x\rangle$	$+1$	$\|\Phi_+\rangle$
$\|+x\rangle$	$\|-x\rangle$	-1	$\|\Phi_-\rangle$
$\|-x\rangle$	$\|+x\rangle$	-1	$\|\Phi_-\rangle$
$\|-x\rangle$	$\|-x\rangle$	$+1$	$\|\Phi_+\rangle$
$\|+y\rangle$	$\|+y\rangle$	-1	$\|\Phi_-\rangle$
$\|+y\rangle$	$\|-y\rangle$	$+1$	$\|\Phi_+\rangle$
$\|-y\rangle$	$\|+y\rangle$	$+1$	$\|\Phi_+\rangle$
$\|-y\rangle$	$\|-y\rangle$	-1	$\|\Phi_-\rangle$

Shown is the parity (and BSM outcome) for each set of valid input states from Alice and Bob. In the case of *Y*-basis inputs, Alice and Bob adjust the sign of their input state depending on whether it was commensurate with an even- or odd-numbered free-precession interval, based on timing information provided by Charlie (Supplementary Information).

Extended Data Table 4 | Quantum-memory-based advantage

	per channel occupancy	per channel occupancy	per channel use	per channel use
X:Y basis bias	50 : 50	99 : 1	50 : 50	99 : 1
Distilled key rate R $[10^{-7}]$	$1.19^{+0.14}_{-0.14}$	$2.33^{+0.28}_{-0.28}$	$2.37^{+0.29}_{-0.28}$	$4.66^{+0.56}_{-0.55}$
$R/R_{\max}$(X:Y)	$2.06^{+0.25}_{-0.25}$	$2.06^{+0.25}_{-0.25}$	$4.13^{+0.50}_{-0.49}$	$4.13^{+0.50}_{-0.49}$
$R/(1.44p_{A\to B})$	$0.71^{+0.09}_{-0.08}$	$1.40^{+0.17}_{-0.17}$	$1.43^{+0.17}_{-0.17}$	$2.80^{+0.34}_{-0.33}$
$1-$confidence level		$1.1^{+0.4}_{-0.3}\times10^{-2}$	$8^{+3}_{-2}\times10^{-3}$	$1.3^{+0.5}_{-0.3}\times10^{-7}$

Overview of distilled key rates R using the asynchronous BSM device and comparison to ideal direct- communication implementations, based on the performance of our network node for $N = 124$ and $\langle n\rangle_m \approx 0.02$. Distillable key rates for $E = 0.110 \pm 0.004$ are expressed in a per-channel-occupancy and per-channel-use normalization for unbiased and biased basis choice (X:Y basis bias) (Methods). Enhancement (fraction of key rates R/R_{max} and $R/(1.44p_{A\to B})$) is calculated versus the linear optics BSM limit ($R_{max}(50{:}50) = p_{A\to B}/2$ for unbiased bases, $R_{max}(99{:}1) = 0.98p_{A\to B}$ with biased bases) and versus the fundamental repeaterless channel capacity[8] ($1.44p_{A\to B}$). Confidence levels for surpassing the latter bound[8] are given in the final row.